iScience

CellPress

Article

Direct-Current Generator Based on Dynamic PN Junctions with the Designed Voltage Output

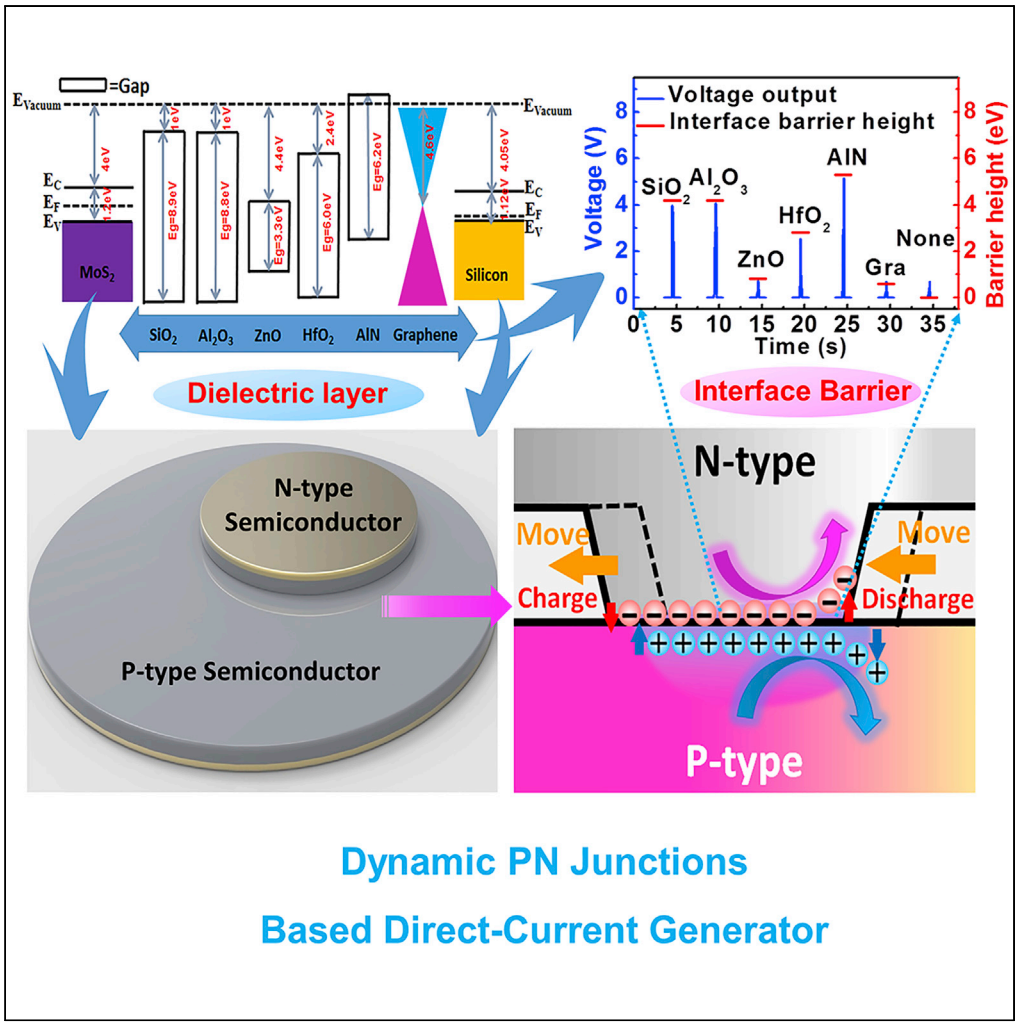

Yanghua Lu, Zhenzhen Hao, Sirui Feng, Runjiang Shen, Yanfei Yan, Shisheng Lin

shishenglin@zju.edu.cn

HIGHLIGHTS

High current density direct-current generator based on dynamic PN junctions

Dynamic equilibrium between establishment and destruction of the depletion layer

Capacitive discharge of PN junction capacitance caused by hot carriers rebounding

Enhance and design voltage numerically by inserting dielectric layer at the interface

Lu et al., iScience *22*, 58–69
December 20, 2019
https://doi.org/10.1016/j.isci.2019.11.004

iScience

CellPress

Article

Direct-Current Generator Based on Dynamic PN Junctions with the Designed Voltage Output

Yanghua Lu,[1] Zhenzhen Hao,[1] Sirui Feng,[1] Runjiang Shen,[1] Yanfei Yan,[1] and Shisheng Lin[1,2,3,*]

SUMMARY

The static PN junction is the foundation of integrated circuits. Herein, we pioneer a high current density generation by mechanically moving N-type semiconductor over P-type semiconductor, named as the dynamic PN junction. The establishment and destruction of the depletion layer causes the redistribution and rebounding of diffusing carriers by the built-in field, similar to a capacitive charge/discharge process of PN junction capacitance during the movement. Through inserting dielectric layer at the interface of the dynamic PN junction, output voltage can be improved and designed numerically according to the energy level difference between the valence band of semiconductor and conduction band of dielectric layer. Especially, the dynamic MoS_2/AlN/Si generator with open-circuit voltage of 5.1 V, short-circuit current density of 112.0 A/m^2, power density of 130.0 W/m^2, and power-conversion efficiency of 32.5% has been achieved, which can light up light-emitting diode timely and directly. This generator can continuously work for 1 h, demonstrating its great potential applications.

INTRODUCTION

The electric energy significantly changed the human society for centuries since the crucial discovery of electromagnetic induction by Michael Faraday, who revealed the connection between magnetism and electricity in 1831 (Faraday, 1831). In the electromagnetic generator, electricity was generated when an electrical conductor passed through a magnetic field. Before that, electric generators were mainly referred to electrostatic generators under the operation principles of electrostatic induction and triboelectric effect (Van Atta et al., 1936). Recently, the piezoelectric and triboelectric nanogenerators have drawn much attention (Wang and Song, 2006; Fan et al., 2012), which were able to convert mechanical and vibrating energy into electricity (Park et al., 2010; Wang, 2013). The triboelectricity utilizes the displacement current in the Maxwell equation, which cannot flow freely through the insulating dielectric materials, limiting its current output density (Wang, 2017). With the rapid development of intelligent and wearable electronic devices putting forward new requirements for in situ energy acquisition technology, it is imperative to search for a portable and integrated electric generator with high current density and stability, which remains as the bottleneck of the current generators without high magnetic field under dark environment (Lin et al., 2019; Wang, 2017; Zhong et al., 2017; Zhu et al., 2013). Hence, a fundamental physical picture distinct from traditional generators is in urgent need to achieve a breakthrough of portable energy harvesting devices (Henniker, 1962; Peng et al., 2017; Baytekin et al., 2013).

The understanding of electron behavior not only advances the information society, but also satisfies the electrical energy requirements for human society. Since the discovery of the PN junction in 1940s (Schottky, 1949), many related applications have been explored such as integrated circuits and optoelectronic devices (Chapin et al., 1954; Li et al., 2015; Lin et al., 2017; Sah et al., 1957; Wu et al., 2018). However, most applications are focused on the static PN structure and there has little exploration on the dynamic PN junction both in information and energy fields (Matyba et al., 2009; Burgener et al., 2011). Recently, high current density direct-current generators have been discovered, which attracts intense attention (Hao et al., 2019; Lin et al., 2019a, 2019b, Liu et al., 2018a, 2018b, 2019, Shao et al., 2016, 2019a, 2019b). Specifically, we have proposed a physical picture based on the semiconductor physics rather than the triboelectric theory at the interface (Hao et al., 2019; Lin et al., 2019a, 2019b). To establish a systematic theoretical framework, a dynamic semiconductor/semiconductor structure, especially the "dynamic PN junction" defined by moving one N-type semiconductor over one P-type semiconductor, should be thoroughly explored, which does not involve metal and insulating polymeric material at all. Herein, a dynamic PN junction-based generator has been achieved, which involves two semiconductors with different Fermi levels (Lu et al., 2019). In the front part of the dynamic PN junction, the electrons and holes will diffuse to p-type and n-type semiconductors, respectively, establishing the built-in electric field. In the rear part of the dynamic PN junction, the

[1]College of Microelectronics, College of Information Science and Electronic Engineering, Zhejiang University, Hangzhou 310027, China

[2]State Key Laboratory of Modern Optical Instrumentation, Zhejiang University, Hangzhou 310027, China

[3]Lead Contact

*Correspondence: shishenglin@zju.edu.cn

https://doi.org/10.1016/j.isci.2019.11.004

diffusing electrons/holes will lose their path for diffusing and then are reflected by the built-in field, thus breaking the balance between diffusing current and drifted current. This carrier transport in the rear part of the dynamic PN junction can be understood by charging capacitance of the PN junction, whereas the rebounding process of the electrons/holes can be understood by the discharging process of the PN junction (Hinchet et al., 2019). When we move N-type GaAs on P-type Si, the destruction of the PN junction will narrow down the space charge region and bound back the space charge to the P-type Si and N-type GaAs, respectively, generating high-energy hot carriers under the ultrahigh built-in electric field. As a result of the rebounding effect, the quasi Fermi level of the dynamic PN junction is different from the equilibrium Fermi level of the static PN junction, leading to the potential difference and output voltage, which is positively related to the barrier height. Notably, the static PN junction is a minority carrier device, where drift and diffusion current balance fight against each other (Lin et al., 2017), whereas the dynamic PN junction is found as a majority carrier device as the majority carriers contribute to the net current output. So the barrier capacitance is the main factor of our dynamic PN junction. In addition, the barrier height of the PN junction can be much larger than the Schottky diode as the Fermi level difference between N-type and P-type semiconductors can be several times that of metal and semiconductor, leading to a higher voltage larger than 1.0 V.

Furthermore, through inserting the dielectric layer into the dynamic PN junction interface, a higher voltage output can be realized, which is delicately designed and numerically calculated according to the energy level difference between the valence band of P-type semiconductor and the valence band of dielectric layer. The electrical properties of static P-i-N structure generator with different thickness and types of insulating layer have been explored (Li et al., 2016; Shewchun et al., 1978). The choice of different kinds of dielectric layer leads to a variable barrier height at the interface, which acts as the barrier for the carriers charging/discharging in P-i-N junction capacitance. With the increasing of barrier height, more electrons and holes with higher energy will be rebounded back and speeded up in the depletion region, which can also be understood from the point view of the discharging process with increased P-i-N barrier capacitance (Maserjian and Zamani, 1982; Lenzlinger and Snow, 1969), leading to enhanced voltage output as high as the energy level difference between the valence band of semiconductor and the conduction band of dielectric layer. Herein, we designed a hot electron-induced dynamic MoS_2/AlN/Si generators with higher open-circuit voltage (V_{oc}) of 5.1 V, high short-circuit current density (J_{sc}) of 112.0 A/m^2 (11.2 mA/cm^2), high power density of 130.0 W/m^2, and high energy-conversion efficiency of 32.5%, which can light up the light-emitting diodes (LEDs) without any external rectifying circuits and energy storage units timely and directly. This dynamic MoS_2/AlN/Si generator can work continuously for 60 min, which demonstrates it can harvest electric energy from the mechanical movement as long as the built-in field dynamically disappears and is re-established. This dynamic PN junction generator also shines in ultrahigh current density, which is orders of magnitude higher than triboelectric nanogenerators (~10^3 times) and piezoelectric nanogenerators (~10^4 times) (Wang, 2017; Wang et al., 2015). Connected in series or in parallel, this dynamic PN junction generator is found to be highly reliable and can effectively increase the output voltage or current. Specifically, two and three dynamic P-Si/N-GaAs generators in series can effectively output a voltage of 6.1 and 9.0 V, respectively, indicating the linear superposition effect and integration potential of our devices. And the current output is positively proportional to the working area but the current density is almost the same under small contact area condition, indicating that the current output can be improved by designing the interface array structure. For convenience, we refer both the dynamic PN junction without inserting dielectric layer and P-i-N junction with insulating layer at the PN interface as the dynamic PN junction. However, in some cases, the P-i-N junction is specifically noted for illustrating the effect of insulating layer.

RESULTS

A Dynamic GaAs/Si Junction-Based Direct Current Generator

As a representative dynamic PN generator, the schematic structure of the dynamic GaAs/Si generator is illustrated in Figure 1A. The N-type GaAs wafer was pressed on the P-type Si substrate compactly with a 6.0 N force, which showed typical rectification behavior with a low leakage current density of 1.5 μA/cm^2 under the bias voltage of −3 V (Figure 1B). The work function of N-type GaAs and P-type Si used here is 4.10 and 5.12 eV (the calculation is listed in Supplemental Information), respectively. Accordingly, since the work function of N-GaAs is smaller than that of P-Si, a built-in electric field will be formed between N-GaAs and P-Si substrates when they contact each other. Primarily, the N-type GaAs was dragged along the surface of the P-type Si and a maximal V_{oc} up to 0.7 V was observed, which was independent of the

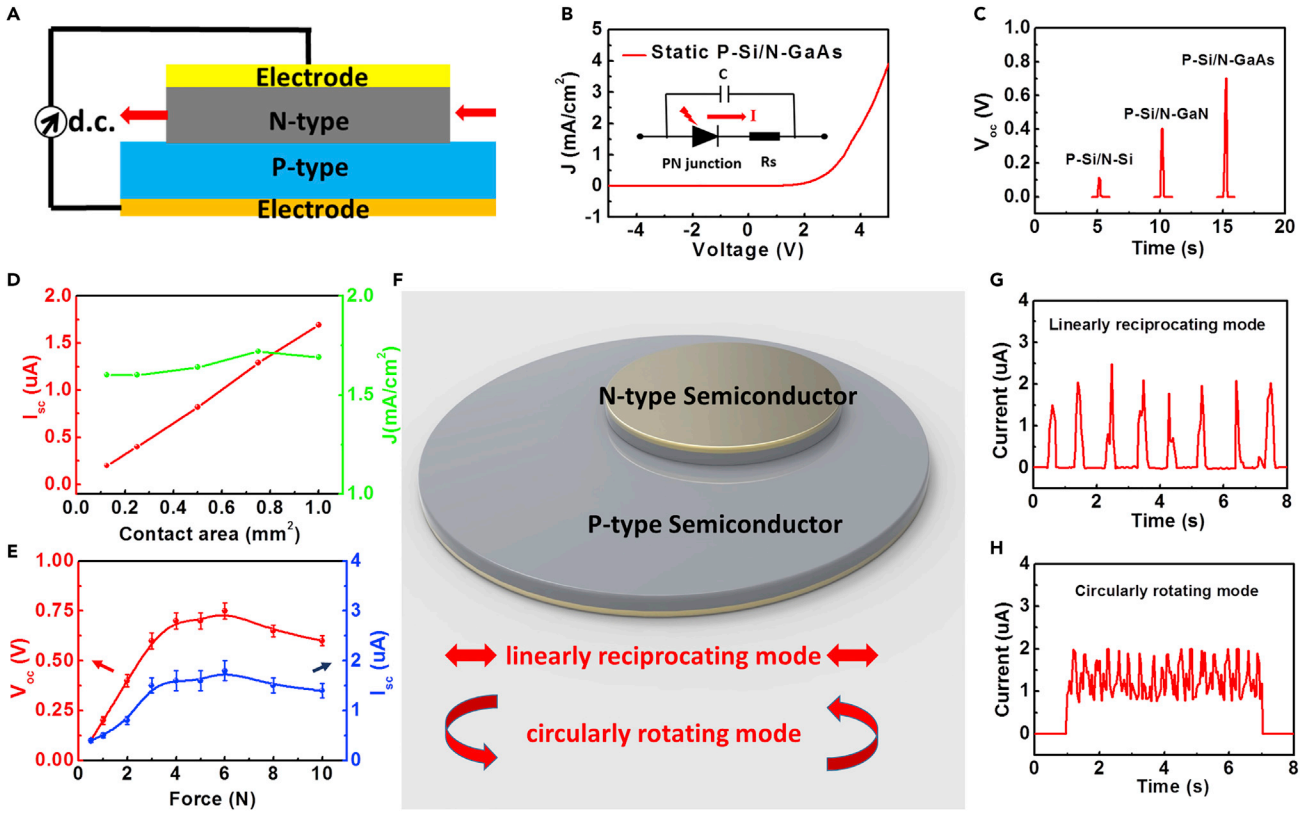

Figure 1. Experimental Designs and Results of the Dynamic PN Generator

(A) The schematic illustration of the dynamic P-Si/N-GaAs generator.

(B) The J-V curve of the static P-Si/N-GaAs junction with a 6.0 N force. The contact area is 1.0 mm^2. Inset: The circuit diagram of P-Si/N-GaAs junction.

(C) The V_{oc} of dynamic P-Si/N-Si, P-Si/N-GaN, P-Si/N-GaAs generator with a speed of 5.0 cm/s and a 6.0 N force.

(D) The I_{sc} and J_{sc} of dynamic P-Si/N-GaAs generator under different contact area, with a 6.0 N force and a speed of 5.0 cm/s.

(E) The V_{oc} and I_{sc} of dynamic P-Si/N-GaAs generator with different force exerted on the junction in a speed of 5.0 cm/s.

(F) Experimental design and 3D diagram for converting mechanical energy into electrical energy by a dynamic PN junction. The bottom inset shows the linearly reciprocating and circularly rotating modes of the generator, respectively.

(G) The I_{sc} of dynamic P-Si/N-GaAs generator under the linearly reciprocating mode with a 6.0 N force and a speed of 5.0 cm/s.

(H) The I_{sc} of dynamic P-Si/N-GaAs generator under circularly rotating mode with a 6.0 N force and a speed of 5.0 cm/s.

All data represent the mean ± SEM. For the line chart in (E), voltage and current were obtained using repeated measures.

working area. The dynamic P-Si/N-Si and P-Si/N-GaN junctions can also output voltage signal as well as the P-Si/N-GaAs junction, among which the V_{oc} of the P-Si/N-GaAs junction is the highest, which is seven times that of the dynamic P-Si/N-Si generator (Figure 1C). The Fermi levels of N-Si and N-GaN are about 4.28 and 4.35 eV (the calculation is listed in Supplemental Information), so the generated voltage direction of P-Si/N-Si and P-Si/N-GaN generators is similar to that of the P-Si/N-GaAs generator, revealing that the voltage output is correlated with the Fermi level location (many other semiconductors are also explored in Figure S1). The noteworthy finding is that only limited noise electricity can be produced when moving one piece of P-type Si over another P-type Si with the same Fermi level (Figure S2), further demonstrating that the voltage output is related with the Fermi level location. Figure 1D shows that the current output is positively proportional to the working area under small contact area condition, indicating the current output can be improved by designing the interface array structure. For the GaAs/Si dynamic PN generator with a working area of 1.0 mm^2 (2 cm × 0.05 mm), a maximal I_{sc} up to 1.8 μA was observed primitively, which was positively related to the movement speed within limits (as shown in Figure S3). The J_{sc} up to 1.8 A/m^2 can be calculated accordingly, which is orders of magnitude higher than that of the reported polymer-based triboelectric nanogenerators (in the order of 10^{-1} A/m^2) and piezoelectric generators (in the order of 10^{-2} A/m^2) (Wang, 2017; Wang et al., 2015). Furthermore, the relationship between the V_{oc}/I_{sc} and the force exerted on the device is explored, as shown in Figure 1E. The V_{oc}/I_{sc} increases and then decreases

with the increase of exerted force, and a force of 6.0 N is found as the optimal choice (Figure 1E), where the N-GaAs and P-Si can achieve the best rectification characteristic (as shown in J-V curves of the P-Si/N-GaAs junction under different forces in Figure S4 and N_{IF} in Supplemental Information). The 3D diagram for converting mechanical energy into electrical energy by the dynamic PN junction is shown in Figure 1F, which can work in linearly reciprocating mode or circularly rotating mode. Figures 1G and 1H show the I_{sc} of the generator in linearly reciprocating mode and circularly rotating mode, respectively. It can be seen that the linear reciprocating mode outputs a pulsed current, which is the result of the inevitable acceleration and deceleration of the GaAs wafer motion. In contrast, when the GaAs wafer is continuously and evenly moving under the circularly rotating mode, it outputs a sustainable direct current.

Work Mechanism Based on Dynamic PN Junction Capacitance

As shown in Equations 1, 2, and 3, the electron current density of the PN junction consists of J_n^{drift} and J_n^{diff}, which is opposite and canceled out. At the static PN junction, the drift current will quickly balance with the diffusion current as the P-type side stably contacts with N-type side, which is equivalent to a PN junction capacitance charge process. The PN junction capacitance is divided into two parts, barrier capacitance and diffusion capacitance. Because our dynamic PN junction works as a majority carrier device rather a minority carrier device like static PN junction, the barrier capacitance is the main factor of the dynamic PN junction. Actually, for the P-Si/N-GaAs junction, the drift and diffusion electron current can be described as follows (Zhang et al., 2011):

$$J_n^{drift} = qnu_n\mathrm{E} \quad \text{(Equation 1)}$$

$$J_n^{diff} = qD_n\nabla n \quad \text{(Equation 2)}$$

$$J_n = J_n^{drift} + J_n^{diff} = qnu_n\mathrm{E} + qD_n\nabla n \quad \text{(Equation 3)}$$

where J_n^{drift}, J_n^{diff}, J_n, μ_n, D_n are the drift electron current, the diffusion electron current, the electron current density, the electron mobility, and the electron diffusion coefficient of GaAs and Si, respectively. E is the built-in electric field, q is the elementary charge, n is the position-dependent electron density in GaAs or Si. When the GaAs wafer moves along the Si substrate, there is a dynamic process of disappearing of the depletion layer in the rear end and the re-establishment of the depletion layer in the front end. In macro scale, the effective working area of the dynamic PN junction is assumed as the contact area of the GaAs wafer and Si substrate during the movement, which remains unchanged. However, the dynamic process of the generation and disappearance of the depletion layer in the dynamic GaAs/Si junction will break up the static carrier distribution equilibrium. The destruction of the PN junction will narrow down the space charge region and reflect the apace electrons/holes, which is equivalent to capacitance discharge process. As schematically shown in Figure 2A, the electrons and holes will be rebounded back to the N-type GaAs and P-type Si, respectively, generating high-energy hot electrons and holes and current output under the acceleration of the strong built-in electric field. The J-V curve of the dynamic N-GaAs/P-Si junction from −5 to 5 V was measured and showed in Figure 2B, where current response oscillates as voltage increases. The destruction of the PN junction leads to the decrease of the basal current density of the dynamic PN junction compared with the static one, as shown by the green line in Figure 2B. There are two reasons for the fluctuation or oscillation of the dynamic J-V curve in Figure 2B, one is the variation of the force applied and the other is the interaction between the reflecting charging carriers and the drifted carriers by external field. The forward bias voltage-induced carriers will bump with the reflecting carriers randomly, which will superpose on this J-V curve of the dynamic N-GaAs/P-Si junction. So this fluctuation is partially caused by the strong interaction between the mechanical energy-induced carriers and electric field-generated carriers of the dynamic PN junction, which provides the platform for using both field energy and mechanical energy. The periodical current oscillation that superposes on this direct-current output can be ascribed to the variation of the force applied on the dynamic PN junction, which behaves as a stable periodicity under the circularly rotating mode. Because our dynamic PN junction works as a majority carrier device rather than a minority carrier device like the static PN junction, the output current density of the dynamic PN junction generator is rather high (Wang, 2017; Wang et al., 2015). The detailed band-gap alignment between P-Si and N-GaAs and transportation of the bounding back electrons and holes are proposed and showed in Figure 2C. The direction of built-in electric field is from N-GaAs to P-Si as a result of electron diffusion from N-GaAs to P-Si. When the N-GaAs wafer is dragged on the P-Si substrate, there is a discharging process of the dynamic PN junction. As a result, the quasi Fermi level of the dynamic PN junction is under non-equilibrium state, different from the equilibrium Fermi level of the static PN junction, leading to the potential difference and output voltage, which is positively related to the interface barrier height.

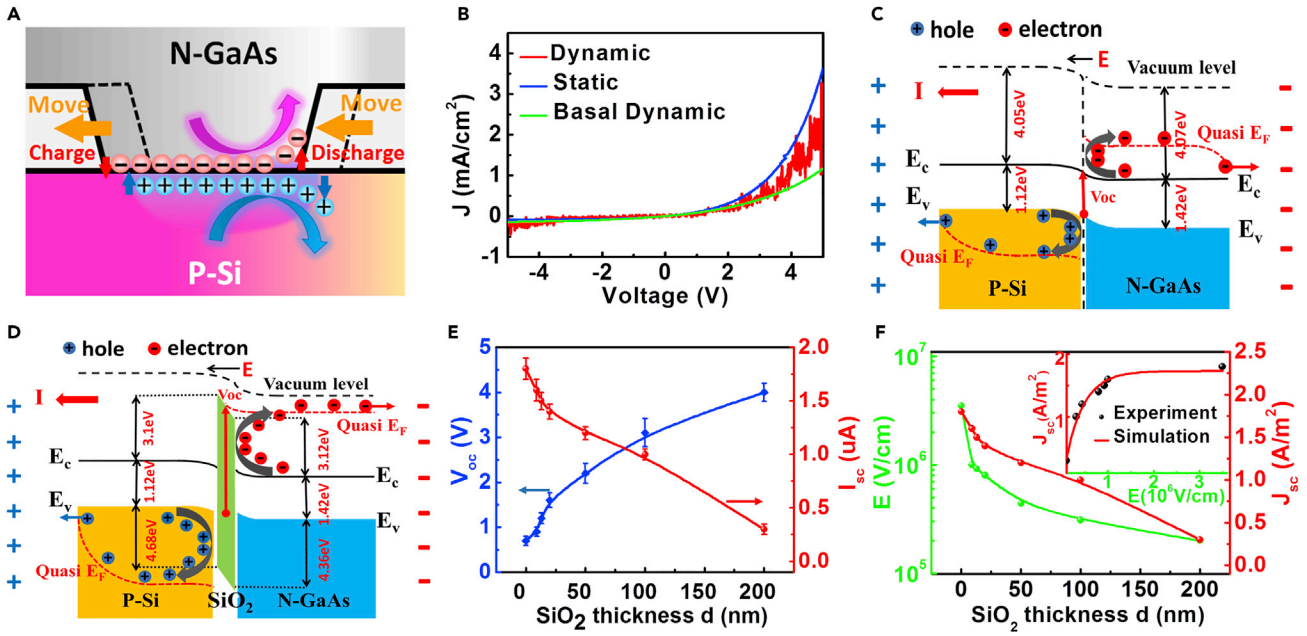

Figure 2. The Physical Mechanism Based on Dynamic PN Junction Capacitance under the Built-in Electric Field in Dynamic PN Junctions

(A) The schematic diagram of the dynamic P-Si/N-GaAs generator.

(B) The J-V curve of the dynamic P-Si/N-GaAs junction with a 6.0 N force. The contact area is 1.0 mm^2. Green: The basal J-V curve of dynamic PN junction. Blue: The J-V curve of static PN junction.

(C) The band diagram and carrier dynamic process of the dynamic P-Si/N-GaAs generator.

(D) The band diagram and carrier dynamic process of the dynamic P-Si/SiO_2/N-GaAs generator.

(E) The V_{oc} and I_{sc} of the dynamic P-Si/N-GaAs generator with a 6.0 N force, a speed of 5.0 cm/s, and SiO_2 thickness of 0/9/13/20/50/100/200 nm. The work area of the P-Si/N-GaAs junction is 1.0 mm^2. Both the V_{oc} and J_{sc} are average value of voltage and current output.

(F) The E and J_{sc} of the dynamic P-Si/N-GaAs generator with SiO_2 thickness of 0/9/13/20/50/100/200 nm. The inset is the simulation of the experimental current density as a function of electric field.

All data represent the mean ± SEM. For the line chart in (E), voltage and current were obtained using repeated measures.

Enhance the Interface Barrier Height by Inserting A Dielectric Layer

Recently, there are some researches on the electron transfer in nanoscale contact electrification between the metal and insulator, which indicates the important role of light and temperature in the charge transfer process of metal-dielectric case (Lin et al., 2019a, 2019b). To eliminate the electrical output caused by temperature, illumination, and humidity changes, we also have carried out experiments on the relationship between the V_{oc} of the dynamic PN junction generator with the humidity, illumination, and temperature of environment. We find that the temperature difference of semiconductors before and after the friction is very limited (Figure S5) and voltage/current output of the dynamic PN generator shows limited change in the humidity environment of 25% or 50% and under different illumination (Figure S6), which indicates that the illumination, humidity, and heat effect are ignorable for outputting electrical signal in our semiconductor-semiconductor case. For the proposed physical picture, the electrical output should be enhanced with the increase of built-in electric field and the interface barrier height of the dynamic PN junction. Therefore, P-type silicon wafers with different thickness (d) of silicon oxide are used here to prove this distinctive current generation mechanism and to reveal the hot carrier kinetic process in dynamic PN junction. We find that this dynamic P-i-N structure generator has a higher voltage output benefited from the increased interface barrier height (Li et al., 2016; Shewchun et al., 1978). As shown in the band diagram of dynamic N-GaAs/SiO_2/P-Si junction (Figure 2D), the barrier height for bounding back charging electrons and holes is largely increased as the conduction/valence bands of SiO_2 are much higher/lower than that of GaAs and Si (Ning et al., 1977), generating a higher interface semiconductor-SiO_2 barrier. The detailed one-dimensional band diagram and rectification characteristic of the P-Si/SiO_2/N-GaAs junction is shown in Figure S7, indicating the increase of the barrier height of the GaAs/SiO_2/Si junction. When we move the N-GaAs wafer along the SiO_2/P-Si substrate, the charging electrons and holes can also be reflected, moving toward the ohmic contact of N-GaAs and P-Si, respectively. The inserted SiO_2 layer can largely suppress

the transfer of electrons and holes, which acts as the barrier capacitance for the carriers charging. With the increasing of barrier height, more hot electrons and holes with higher energy will be charged and discharged in the barrier capacitance, leading to enhanced voltage output as high as the energy level difference between the valence band of semiconductor and the conduction band of dielectric layer. As shown in Figure 2E, the average V_{oc} and I_{sc} of the dynamic P-Si/N-GaAs junction with the SiO_2 thickness of 0/9/13/20/50/100/200 nm are 0.7/0.9/1.2/1.6/2.2/3.1/4.0 V and 1.8/1.6/1.5/1.4/1.2/1.0/0.3 μA, respectively.

The P-Si/SiO_2/N-GaAs generator is equivalent to a P-i-N capacitor, among which the P-Si and N-GaAs work as capacitor plate. The hot electrons and holes are generated under the large built-in electric field at the interface during the discharging process, which is decreased with SiO_2 layer thickness. As a result of the high-energy hot carriers, the voltage output is near the difference of the valence band of P-type Silicon and conduction band of SiO_2, which is near 4.2 V as observed in the case of 200 nm SiO_2 in Figure S8 (under the large built-in electric field E as high as 2×10^5 V/cm). With the decrease of electric field E, the possibility of hot carriers generated by the reflecting process is exponentially decaying; thus, a much lower current density was observed for the case of thick SiO_2 that existed at the interface between P and N semiconductor, as shown in Figure 2F. It is confirmed experimentally that the voltage is still enhanced and even larger than the Fermi level difference between N- and P-type semiconductors when the thickness of the insulating layer is larger than 100 nm. It is inferred that the impact ionization should lead to the current transport through the insulating layer (Dervos et al., 1991; Kim and Rudd, 1994; Hwang et al., 1996; Solomon and Klein, 1975; Feng et al., 2019), whereas other transportation processes such as inelastic hopping also cannot be neglected (Xu et al., 1990, 1995; Vecchio et al., 2019), which will be studied in the following works. It is reasonable that some rebounded hot electrons/holes can involve in the impact ionization, since there are ultrahigh built-in electric field ($E \approx 3 \times 10^5$ V/cm for the case of 100 nm SiO_2 as shown in Figure 2F). The high-energy hot electrons are caused by the severely bounding back effect by the large internal field at the interface, leading to the impact ionization of the thick SiO_2 layer as high as 100 nm, causing the current output. As shown in the inset of Figure 2F, the simulation of the experimental current density as a function of electric field shows the current density decay exponentially while the electric field decreases (the detail is listed in Supplemental Information), which supports the phenomenon of conducting current by impact ionization through an insulator under an extremely high electric field (Solomon and Klein, 1975; Kashat and Klein, 1977; DiStefano and Shatzkes, 1974; Glover, 1975; Konstantinov et al., 1998; Raghunathan and Baliga, 1998). The mathematical formula of this dependence can be described by: $J = 1.73 - 1.79 \times e^{-\frac{E}{393000}}$, indicating theoretical short-circuit current density of the dynamic P-Si/SiO_2/N-GaAs generator is as high as 1.73 A/m^2, similar to the experimental result of 1.8 A/m^2. The demonstration of impact ionization-induced current transport further confirms the hot electron/hole production in the dynamic PN generator.

The Quantitative Relationship between Band-Gap Alignments of Semiconductor-Insulator-Semiconductor Structure and Voltage Output

Figure 3A shows the voltage output of this dynamic P-Si/SiO_2/N-GaAs generator in the circularly rotating mode, which can output a continual voltage as high as 3.1 V under the consistent movement. In addition, the V_{oc} outputs of the dynamic P-Si/SiO_2/N-GaAs generator in parallel, two-series, and three-series are 3.1/6.1/9.0 V, indicating the linear superposition effect and integration potential of our devices, which can effectively enhance its voltage output and expand its applications. Furthermore, we use the layered semiconductors such as MoS_2 and achieve a dynamic P-Si/MoS_2 junction with ultrafast carrier dynamics process to illustrate the detailed carrier transportation at the interface (Jin et al., 2018; Lin et al., 2015; Liu et al., 2018; Wu et al., 2018; Xu et al., 2016). The electrons and holes in the dynamic P-Si/MoS_2 junction can also be continuously rebounded back by the built-in electric field during the discharge process, generating hot carriers and stable voltage output. As shown in Figure 3B, the average voltage and current output of the dynamic MoS_2/Si generator with a working area of 0.05 mm^2 and different resistivity of Si substrate are 0.7/1.2/1.5/1.6/1.7 V and 120.1/70.4/38.1/24.0/16.5 A/m^2, respectively. The higher carrier concentration of the silicon wafer leads to a higher current output but lower voltage output, which is attributed to the larger built-in electric field. The built-in electric field is associated with the concentration of electrons and holes of semiconductors at each side. With the increase of the carrier concentration, the built-in electric field is enhanced, generating more hot carriers in the interface thus increasing the current output. At the same time, the barrier height of the MoS_2/Si junction decreases when the carrier concentration increases, which is due to the carriers transfer between MoS_2 and Si, leading to the decrease of voltage output. As a result of the ultrahigh built-in electric field, these hot carriers can locate at the quasi Fermi level higher than

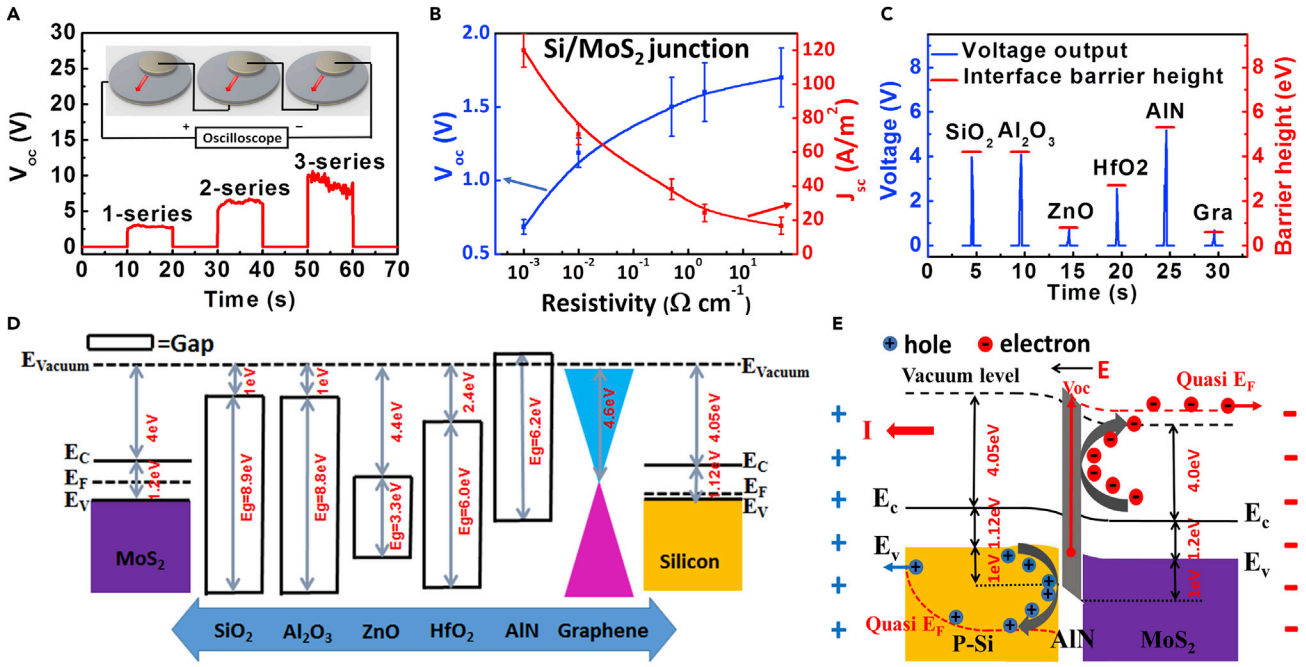

Figure 3. The Confirmatory Experiment Based on Dynamic P-i-N Junctions

(A) The V_{oc} of the dynamic P-Si/100 nm-SiO_2/N-GaAs generator in one-series, two-series, and three-series with a 6.0 N force, a speed of 5.0 cm/s. Inset: The schematic image of series connection of the dynamic PN junctions.

(B) The voltage and current output of dynamic MoS_2/Si generator with different resistivity of Si substrate.

(C) The relationship between the voltage output and interface barrier height.

(D) One-dimensional band alignment of conduction and valence band edges for various dielectric layers (SiO_2, Al_2O_3, ZnO, HfO_2, AlN, Graphene) and semiconductors (Si, MoS_2).

(E) The band diagram and carrier dynamic process of the dynamic P-Si/AlN/MoS_2 generator.

All data represent the mean ± SEM. For the line chart in (B), voltage and current were obtained using repeated measures.

the equilibrium Fermi level of semiconductor, leading to the output voltage being higher than the Fermi level difference of two semiconductors.

To quantitatively reveal the physical mechanism of hot carriers effect in the interface barrier between P-type and N-type semiconductors, various interface dielectric layers are inserted into the dynamic PN junction generator, respectively. The detailed relationship between the voltage output and interface barrier height is shown in Figure 3C. The average voltage output of various dynamic PN junctions with the barrier height of Si and SiO_2/Al_2O_3/ZnO/HfO_2/AlN/graphene interface barrier of 4.2/4.2/0.8/2.8/5.3/0.6 eV is 4.0/4.1/0.7/2.5/5.1/0.7 V, respectively. The one-dimensional band alignment of conduction and valence band edges for various dielectric layers (SiO_2, Al_2O_3, ZnO, HfO_2, AlN, graphene) and semiconductors (Si, MoS_2) is shown in Figure 3D (Lin et al., 2015; Xu et al., 2015; Liu et al., 2005). According to the band structure relativities, the AlN layer with negative electron affinity behaved the highest barrier height, which is supposed to achieve the highest voltage output according to the above-mentioned physical mechanism based on the hot electrons transport induced by the ultrahigh built-in electric field in the dynamic PN structure (Liu et al., 2005). As shown in the band diagram of the dynamic P-Si/AlN/MoS_2 junction (Figure 3E), the hot carriers will be rebounded back to the P-Si and MoS_2 in the effect of interface barrier, leading to a stable potential difference and voltage output between two electrodes. The inserted AlN layer can largely enhanced the barrier height, and more high-energy hot carriers will charge and discharge in the interface of two semiconductors, leading to enhanced voltage output as high as the energy level difference between the valence band of Si and the conduction band of AlN. As a result of the continuous discharging process, the quasi Fermi level of the dynamic PN junction is different from the equilibrium Fermi level of the static PN junction and a voltage output as high as 5.1 V has been achieved. This experimental result is in accordance with our expectation, indicating the validity of our proposed physical mechanism. The rectification characteristic of the dynamic P-Si/AlN/MoS_2 junction from −5 to 5 V is also measured. As shown in Figure S9, the interfacial carrier dynamic process

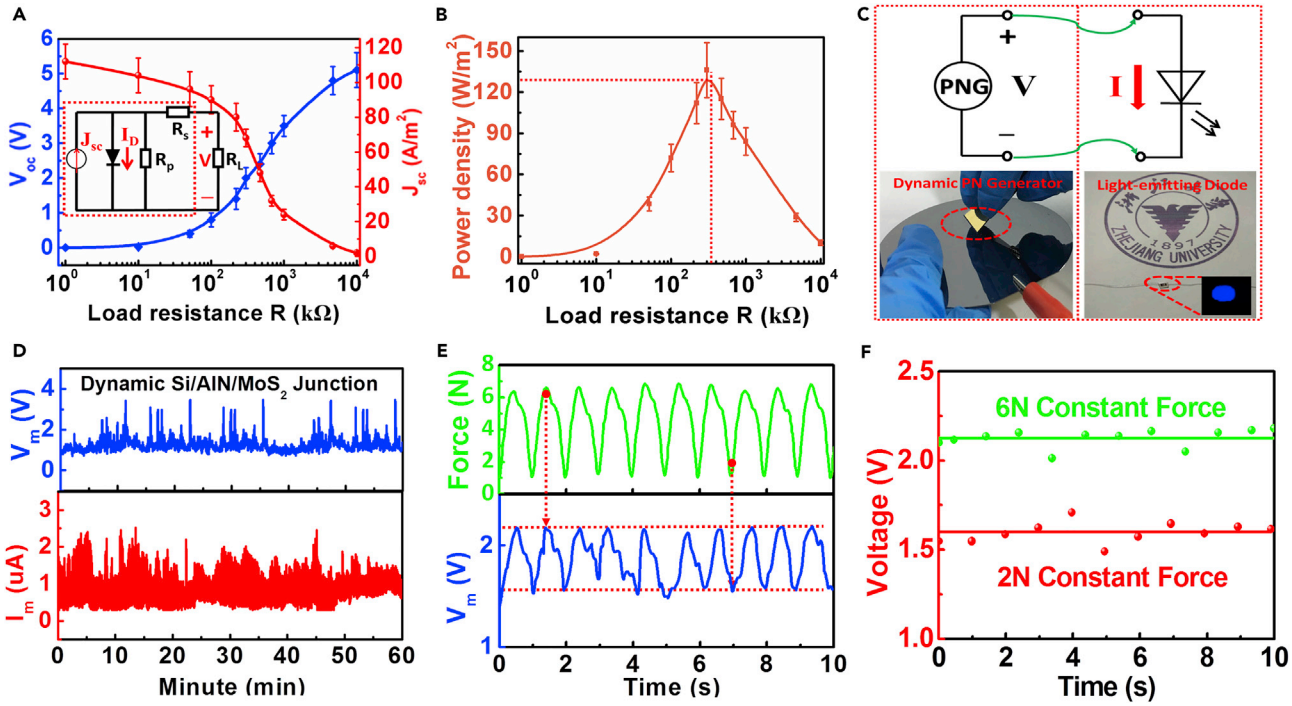

Figure 4. The Electrical Properties of Dynamic P-Si/AlN/MoS_2 Generator and Its Application

(A) V_{oc} and J_{sc} output as a function of electrical load R. Both the V_{oc} and J_{sc} are the average value of voltage and current output. Inset: equivalent circuit.

(B) The power density output as a function of electrical load R.

(C) The circuit diagram of the LED lighting experiment and pictures taken from video to show the luminance of an LED powered by our dynamic PN generator.

(D) The direct voltage and current output of the dynamic P-Si/AlN/MoS_2 generator for 60 min continuously, with an electrical load R of 360 kΩ.

(E) The time-varying force applied and corresponding direct voltage output of the dynamic PN junction.

(F) The linear fitting direct voltage output of the dynamic PN junction under the constant force of 2 and 6 N.

All data represent the mean ± SEM. For the line chart in (A) and (B), voltage and current were obtained using repeated measures.

See also Video S1.

varies when the P-Si/AlN/MoS_2 contact is under the dynamic process, which helps testifying the above-proposed theory. As the graphene is monolayer thick, the built-in electric field of the PN junction cannot be screened by the graphene layer (Zhong et al., 2017) and its impact on the junction capacitance is minimal (the rectification characteristic of Si/graphene/MoS_2 junction is shown in Figure S10). As monolayer graphene cannot screen the electric field (Zhong et al., 2017), the barrier height of the Si/graphene/MoS_2 junction is almost unchanged; thus, the voltage output of the dynamic P/graphene/N junction should be the same as that of the dynamic P/N junction. According to the experimental result (Figure 3E), the MoS_2/Si and MoS_2/graphene/Si output the similar voltage, concluding that the physical picture of the rebounding effect under capacitance discharging process of the dynamic PN junction is self-consistent.

Potential Practical Applications and Future Outlook of Our Dynamic P-Si/AlN/MoS_2 Junction

Finally, a V_{oc} as high as 5.1 V and the average J_{sc} as high as 112.0 A/m^2 can be achieved, which is about three orders of magnitude higher than that of the reported triboelectric nanogenerators (Wang, 2017; Wang et al., 2015). To demonstrate the power output of our generator, the voltage and current outputs as a function of electrical load R have been investigated and shown in Figure 4A. As shown in the equivalent circuit diagram of the dynamic PN junction (inset of Figure 4A), its working circuit consists of a series resistance (R_s), a recombination generated parallel resistance (R_p), and a load resistance (R_L). An increasing voltage and decreasing current density can be measured with the increase of load resistance. The power conversion efficiency of the dynamic PN junction generator can be expressed as below:

$$\mathrm{PCE} = \frac{P_{max}}{P_{in}} = \frac{V_{oc} \times J_{sc} \times FF}{P_{in}} = \frac{V_{max} \times J_{max}}{P_{in}} = \frac{V_{max} \times J_{max}}{F \times v} \qquad \text{(Equation 4)}$$

where V_{oc} is the open-circuit voltage of the generator and J_{sc} is the short-circuit current density of the generator. FF is the fill factor of the generator. V_{max} is the working voltage of the generator under the maximum power output and J_{max} is the working current density of the generator under the maximum power output. F is the force of friction between two semiconductors and v is the moving speed of the semiconductor wafer. We should emphasize that our output power is calculated with the average working voltage and current density of the direct-current generator in 8.0 s and 200 points. According to Equation 4, the power density output as a function of electrical load R_L has also been investigated and shown in Figure 4B. The peak power density about 130.0 W/m^2 can be found around R_L equals to 360 kΩ, which is close to the internal resistance of the PN junction (R_s + R_p). And the energy-conversion efficiency of the moving Si/MoS_2 junction generator can be calculated to be about 32.5% (the calculation is listed in Supplemental Information).

To explore the advantages of our dynamic PN junction generator and its potential practical applications, we use the electricity generated by our devices to light up a blue LED without any external rectifying circuits and energy storage units directly (the picture of experimental model is shown in Figure S11). This LED can be lit up only when the drive voltage is over 2.7 V. Each of MoS_2/AlN/Si generators can provide a nearly 5.1 V voltage output, which can be used to provide enough voltage output for lighting a blue LED. So this dynamic MoS_2/AlN/Si generator can light up the blue LED as shown in Video S1, "blue LED lighting experiment," related to Figure 4C (the circuit diagram of the LED lighting experiment is shown in Figure 4C). The blue light LED is lighted simultaneously with the movement of the PN junction, indicating the output of a continuous direct current (the right inset). Figure 4C shows the picture of the LED powered by our dynamic PN generator. Compared with the conventional triboelectric nanogenerator with pulsed alternating current output characteristics, this dynamic PN junction generator realizes constant current output based on the physical mechanism as mentioned earlier, which is demonstrated to power LED directly without any external rectifying circuits and energy storage units, providing a feasible way to meet the increasing demand of *in situ* energy acquisition technology.

Notably, as MoS_2 is a lubricating material, the dynamic P-Si/AlN/MoS_2 PN junction generator shows long-term continuous electricity generation. As shown in the direct and continuous voltage and current output of the dynamic P-Si/AlN/MoS_2 with an electrical load R_L of 360 kΩ (Figure 4D), this dynamic P-Si/AlN/MoS_2 generator can work continuously for 60 min, demonstrating the proposed mechanism and potential applications of the dynamic PN generator. However, there are some slight oscillations and degradation during the movement. The current oscillation that superposes on this direct-current output can be explained by the variation of the force applied on the dynamic PN junction. To prove the electric oscillation is caused by the force change, we measured the voltage output and corresponding pressure applied in dynamic PN junction synchronously, which both behave a stable periodicity under the circularly rotating mode (Figure 4E). And the maximum peaks and minimum peaks correspond one by one with almost the same amplitudes, indicating the positive correlation of the force and voltage output. On this basis, we demonstrate a pressure sensor, which outputs the periodic voltage signal under a periodic force source. Furthermore, through the linear fitting simulation method, a continuous and smooth output can be achieved under the unique pressure of 2 and 6 N, indicating that a continuous stabilized voltage output can be realized under a constant force (Figure 4F). On the other hand, we attribute the direct current output degradation of the dynamic P-Si/AlN/MoS_2 generator after the long-term work to the residual of lamellar MoS_2 on the surface, which can be easily removed with alcohol wiping. As shown in Figure S12, scanning electron microscope images of the P-Si/AlN surface at different time points are measured to show the surface morphology change of the AlN/P-Si substrate. As a typical layered semiconductor material, the surface of MoS_2 does not show obvious change during the movement, leading to the continuous voltage and current output before the continuous operation of 10 min. However, with the long-term work, it becomes common that P-Si/AlN with higher hardness will slightly wear MoS_2 with lower hardness, leading to the wear of the lamellar MoS_2, causing the slight degradation of the dynamic P-Si/AlN/MoS_2 generator. Those MoS_2 can be easily removed with alcohol wiping and the performance of the generator can be recovered, which indicates that the dynamic PN junction generator is "reusable." However, more follow-on studies are necessary for this dynamic PN junction direct-current generator to be applied in specific application field.

DISCUSSION

In this article, we have pioneered a direct-current generator based on the dynamic PN junction, where two semiconductors with different Fermi levels move with each other, such as the N-GaAs/P-Si junction. The mechanism is proposed based on the rebounding effect of otherwise diffused electrons/holes as well as the capacitive charge/discharge process of the PN junction capacitance during the movement, which is

originated from the establishment and disappearing of the depletion layer. Through inserting a dielectric layer at the interface of the PN junction, the output voltage can be delicately improved and designed numerically according to the energy level difference between the valence band of P-type semiconductor and the conduction band of dielectric layer. Herein, a dynamic PN generator with a high voltage of 5.1 V, current density of 112.0 A/m^2 (11.2 mA/cm^2), power density of 130.0 W/m^2 and energy-conversion efficiency of 32.5% has been realized based on the MoS_2/AlN/Si structure, which can power the LED without any external circuits timely and directly. The voltage, current, and output power of the dynamic PN generator can be further enhanced through designing the interface array structure of semiconductors by being connected in series or in parallel and optimizing the carrier barrier layer of the dynamic PN junction. Especially, this dynamic P-Si/AlN/MoS_2 generator can work continuously for 60 min, demonstrating the proposed mechanism and potential applications of the dynamic PN generator. This dynamic PN generator with sufficient current density has many promising applications in many fields where mechanical energy is available.

Limitations of the Study

Dynamic PN junctions generate high current density direct current by mechanically moving N-type semiconductor over P-type semiconductor. In some cases, semiconductor with higher hardness will slightly wear semiconductor with lower hardness, leading to the wear of the semiconductor with lower hardness, causing the slight degradation of the dynamic PN generator, which we overcome through using layered semiconductor material such as MoS_2 in this article. However, more follow-on studies are necessary for this dynamic PN junction direct-current generator to be applied in specific application field, especially in the low-frequency disordered mechanical motion, such as the human motion and wind and ocean energy.

METHODS

All methods can be found in the accompanying Transparent Methods supplemental file.

SUPPLEMENTAL INFORMATION

Supplemental Information can be found online at https://doi.org/10.1016/j.isci.2019.11.004.

ACKNOWLEDGMENTS

S.L. thanks the support from the National Natural Science Foundation of China (No. 51202216, 51502264, and 61774135) and Special Foundation of Young Professor of Zhejiang University (Grant No. 2013QNA5007).

AUTHOR CONTRIBUTIONS

S.L. designed the experiments, analyzed the data, and conceived all the works. Y.L. carried out the experiments, discussed the results, and wrote the paper. S.F., Z.H., and R.S. discussed the results and assisted with experiments. All authors contributed to the writing of the paper.

DECLARATION OF INTERESTS

The authors declare no conflicts of interests.

Received: July 4, 2019
Revised: October 25, 2019
Accepted: November 1, 2019
Published: December 20, 2019

REFERENCES

Baytekin, H.T., Baytekin, B., Hermans, T.M., Kowalczyk, B., and Grzybowski, B.A. (2013). Control of surface charges by radicals as a principle of antistatic polymers protecting electronic circuitry. Science *341*, 1368–1371.

Burgener, I.R.H., Felix, R.L., & Renlund, G.M.. (2011). Dynamic pn junction growth. U.S. Patent 7,935,616.

Chapin, D.M., Fuller, C., and Pearson, G. (1954). A new silicon p-n junction photocell for converting solar radiation into electrical power. J. Appl. Phys. *25*, 676–677.

Dervos, C., Bourkas, P.D., and Kagarakis, C.A. (1991). Charge transport trough a "metal-thick insulator metal" structure during impulse voltage excitation. J. Electrostat. *26*, 121–132.

DiStefano, T.H., and Shatzkes, M. (1974). Impact ionization model for dielectric instability and breakdown. Appl. Phys. Lett. *25*, 685–687.

Fan, F.R., Tian, Z.Q., and Wang, Z.L. (2012). Flexible triboelectric generator. Nano Energy *1*, 328–334.

Faraday, M.X.V., II (1831). On a peculiar class of acoustical figures; and on certain forms assumed

by groups of particles upon vibrating elastic surfaces. Philos. Trans. R. Soc. Lond. *121*, 299–340.

Feng, S.R., Dong, B.Z., Lu, Y.H., Yin, L.F., Wei, B.L., Wang, J.B., and Lin, S.S. (2019). Graphene/p-AlGaN/p-GaN electron tunnelling light emitting diodes with high external quantum efficiency. Nano Energy *60*, 836–840.

Glover, G.H. (1975). Charge multiplication in Au-SiC (6H) Schottky junctions. J. Appl. Phys. *46*, 4842.

Hao, Z.Z., Jiang, T.M., Lu, Y.H., Feng, S.R., Shen, R.J., Yao, T.Y., and Yan, Y.F. (2019). Co-harvesting light and mechanical energy based on dynamic metal/perovskite Schottky junction. Matter *1*, 639–649.

Henniker, J. (1962). Triboelectricity in polymers. Nature *196*, 474.

Hinchet, R., Yoon, H.J., Ryu, H., Kim, M.K., Choi, E.K., Kim, D.S., and Kim, S.W. (2019). Transcutaneous ultrasound energy harvesting using capacitive triboelectric technology. Science *365*, 491–494.

Hwang, W., Kim, Y.K., and Rudd, M.E. (1996). New model for electron-impact ionization cross sections of molecules. J. Chem. Phys. *104*, 2956–2966.

Jin, C.H., Ma, E.Y., Karni, O., Regan, E.C., Wang, F., and Heinz, T.F. (2018). Ultrafast dynamics in van der Waals heterostructures. Nat. Nanotechnol. *13*, 994.

Kashat, I., and Klein, N. (1977). Current runaway in insulators affected by impact ionization and drift. J. Appl. Phys. *48*, 5217–5226.

Kim, Y.K., and Rudd, M.E. (1994). Binary-encounter-dipole model for electron-impact ionization. Phys. Rev. A *50*, 3954.

Konstantinov, A.O., Wahab, Q., Nordell, N., and Lindefelt, U. (1998). Study of avalanche breakdown and impact ionization in 4H silicon carbide. J. Electron. Mater. *27*, 335–341.

Lenzlinger, M., and Snow, E. (1969). Fowler-Nordheim tunneling into thermally grown SiO_2. J. Appl. Phys. *40*, 278–283.

Li, X.Q., Chen, W.C., Zhang, S.J., Wu, Z.Q., Wang, P., Xu, Z.J., Chen, H.S., Yin, W.Y., Zhong, H.K., and Lin, S.S. (2015). 18.5% efficient graphene/GaAs van der Waals heterostructure solar cell. Nano Energy *16*, 310–319.

Li, X.Q., Lin, S.S., Lin, X., Xu, Z.J., Wang, P., Zhang, S.J., Zhong, H.K., Xu, W.L., Wu, Z.Q., and Fang, W. (2016). Graphene/h-BN/GaAs sandwich diode as solar cell and photodetector. Opt. Express *24*, 134–145.

Lin, S.S., Li, X.Q., Wang, P., Xu, Z.J., Zhang, S.J., Zhong, H.K., Wu, Z.Q., Xu, W.L., and Chen, H.S. (2015). Interface designed MoS_2/GaAs heterostructure solar cell with sandwich stacked hexagonal boron nitride. Sci. Rep. *5*, 15103.

Lin, S.S., Lu, Y.H., Feng, S.R., Hao, Z.Z., and Yan, Y.F. (2019a). A high current density direct-current generator based on a moving van der Waals Schottky diode. Adv. Mater. *31*, 1804398.

Lin, S.S., Lu, Y.H., Xu, J., Feng, S.R., and Li, J.F. (2017). High performance graphene/semiconductor van der Waals heterostructure optoelectronic devices. Nano Energy *40*, 122–148.

Lin, S.S., Shen, R.J., Yao, T.Y., Lu, Y.H., Feng, S.R., Hao, Z.Z., Zheng, H.N., Yan, Y.F., and Li, E.P. (2019). Surface States Enhanced Dynamic Schottky Diode Generator with Extremely High Power Density Over 1000 W m^{-2}. Advanced Science, 1901925, .In press. https://doi.org/10.1002/advs.201901925.

Lin, S.Q., Xu, L., Xu, C., Chen, X.Y., Wang, A.C., Zhang, B.B., Lin, P., Yang, Y., Zhao, H.B., and Wang, Z.L. (2019b). Electron transfer in nanoscale contact electrification: effect of temperature in the metal-dielectric case. Adv. Mater. *31*, 1808197.

Lin, S.Q., Xu, L., Zhu, L.P., Chen, X.Y., and Wang, Z.L. (2019c). Electron transfer in nanoscale contact electrification: photon excitation effect. Adv. Mater. *0*, 1901418.

Liu, C., Hu, Z., Wu, Q., Wang, X.Z., Chen, Y., Lin, W.W., Sang, H., Deng, S.Z., and Xu, N.S. (2005). Synthesis and field emission properties of aluminum nitride nanocones. Appl. Surf. Sci. *251*, 220–224.

Liu, J., Goswami, A., Jiang, K.R., Khan, F., Kim, S., McGee, R., Li, Z., Hu, Z.Y., Lee, J., and Thundat, T. (2018a). Direct-current triboelectricity generation by a sliding Schottky nanocontact on MoS_2 multilayers. Nat. Nanotechnol. *13*, 112–116.

Liu, J., Miao, M.M., Jiang, K.R., Khan, F., Goswami, A., McGee, R., Li, Z., Nguyen, L., Hu, Z.Y., Lee, J., et al. (2018b). Sustained electron tunneling at unbiased metal-insulator-semiconductor triboelectric contacts. Nano Energy *48*, 320–326.

Liu, J., Jiang, K.R., Nguyen, L., Li, Z., and Thundat, T. (2019). Interfacial friction-induced electronic excitation mechanism for tribo-tunneling current generation. Mater. Horiz. *6*, 1020–1026.

Lu, Y.H., Feng, S.R., Hao, Z.Z., Shen, R.J., and Lin, S.S. (2019). High Performance Direct-Current Generator Based on Dynamic PN Junctions. Arxiv preprint1901.00701, arXiv:1901.00701.

Maserjian, J., and Zamani, N. (1982). Behavior of the Si/SiO_2 interface observed by Fowler-Nordheim tunneling. J. Appl. Phys. *53*, 559–567.

Matyba, P., Maturova, K., Kemerink, M., Robinson, N.D., and Edman, L. (2009). The dynamic organic p-n junction. Nat. Mater. *8*, 672.

Ning, T., Osburn, C., and Yu, H. (1977). Emission probability of hot electrons from silicon into silicon dioxide. J. Appl. Phys. *48*, 286–293.

Park, K.I., Xu, S., Liu, Y., Hwang, G.T., Kang, S.J.L., Wang, Z.L., and Lee, K.J. (2010). Piezoelectric $BaTiO_3$ thin film nanogenerator on plastic substrates. Nano Lett. *10*, 4939–4943.

Peng, J., Kang, S.D., and Snyder, G.J. (2017). Optimization principles and the figure of merit for triboelectric generators. Sci. Adv. *3*, 8576.

Raghunathan, R., and Baliga, B.J. (1998). Role of defects in producing negative temperature dependence of breakdown voltage in SiC. Appl. Phys. Lett. *72*, 3196–3198.

Sah, C.T., Noyce, R.N., and Shockley, W. (1957). Carrier generation and recombination in pn junctions and pn junction characteristics. Proc. IRE *45*, 1228–1243.

Schottky, W. (1949). The theory of p-n junctions in semiconductors and p-n junction transistors. Bell Syst. Tech. J. *28*, 435–489.

Shao, H., Fang, J., Wang, H.X., Dai, L.M., and Lin, T. (2016). Polymer-metal Schottky contact with direct-current outputs. Adv. Mater. *28*, 1461–1466.

Shao, H., Fang, J., Wang, H.X., Niu, H.T., Zhou, H., Cao, Y.Y., Chen, F.Y., Fu, S., and Lin, T. (2019a). Schottky direct-current energy harvester with large current output density. Nano Energy *62*, 171–180.

Shao, H., Fang, J., Wang, H.X., Zhou, H., Niu, H.T., Chen, F.Y., Yan, G.L., Fu, S., Cao, Y.Y., and Lin, T. (2019b). Doping effect on conducting polymer-metal Schottky DC generators. Adv. Electron. Mater. *5*, 1800675.

Shewchun, J., Dubow, J., Myszkowski, A., and Singh, R. (1978). The operation of the semiconductor-insulator-semiconductor (SIS) solar cell: Theory. J. Appl. Phys. *49*, 855–864.

Solomon, P., and Klein, N. (1975). Impact ionization in silicon dioxide at fields in the breakdown range. Solid State Commun. *17*, 1397–1400.

Van Atta, L.C., Northrup, D.L., Van Atta, C.M., and Van De Graaff, R.J. (1936). The design, operation, and performance of the round hill electrostatic generator. Phys. Rev. *49*, 761–776.

Vecchio, M.A., Meddeb, A.B., Ounaies, Z., and Lanagan, M.T. (2019). Conduction through plasma-treated polyimide: analysis of high-field conduction by hopping and Schottky theory. J. Mater. Sci. *54*, 10548–10559.

Wang, Z.L. (2013). Triboelectric nanogenerators as new energy technology for self-powered systems and as active mechanical and chemical sensors. ACS Nano *7*, 9533–9557.

Wang, Z.L. (2017). On Maxwell's displacement current for energy and sensors: the origin of nanogenerators. Mater. Today *20*, 74–82.

Wang, Z.L., and Song, J. (2006). Piezoelectric nanogenerators based on zinc oxide nanowire arrays. Science *312*, 242–246.

Wang, Z.L., Chen, J., and Lin, L. (2015). Progress in triboelectric nanogenerators as a new energy technology and self-powered sensors. Energ. Environ. Sci. *8*, 2250–2282.

Wu, J.H., Lu, Y.H., Feng, S.R., Wu, Z.Q., Lin, S.Y., Hao, Z.Z., Yao, T.Y., Li, X.M., Zhu, H.W., and Lin, S.S. (2018a). The interaction between quantum dots and graphene: the applications in graphene-based solar cells and photodetectors. Adv. Func. Mater. *28*, 1804712.

Wu, Z.Q., Yang, J.L., Mnajunath, N.K., Zhang, Y.J., Feng, S.R., Lu, Y.H., Wu, J.H., Zhao, W.W., Qiu, C.Y., Li, J.F., and Lin, S.S. (2018b). Gap-mode surface-plasmon-enhanced photoluminescence and photoresponse of MoS_2. Adv. Mater. *30*, 1706527.

Xu, Y., Matsuda, A., and Beasley, M.R. (1990). Role of inelastic effects on tunneling via localized states in metal-insulator-metal tunnel junctions. Phys. Rev. B *42*, 1492.

Xu, Y.Z., Ephron, D., and Beasley, M.R. (1995). Directed inelastic hopping of electrons through metal-insulator-metal tunnel junctions. Phys. Rev. B *52*, 2843.

Xu, S.Z., Jacobs, R.M., Nguyen, H.M., Hao, S.Q., Mahanthappa, M., Wolverton, C., and Morgan, D. (2015). Lithium transport through lithium-ion battery cathode coatings. J. Mater. Chem. A *3*, 17248–17272.

Xu, Z.J., Lin, S.S., Li, X.Q., Zhang, S.J., Wu, Z.Q., Xu, W.L., Lu, Y.H., and Xu, S. (2016). Monolayer MoS_2/GaAs heterostructure self-driven photodetector with extremely high detectivity. Nano Energy *23*, 89–96.

Zhang, Y., Liu, Y., and Wang, Z.L. (2011). Fundamental theory of piezotronics. Adv. Mater. *23*, 3004–3013.

Zhong, H.K., Xia, J., Wang, F.C., Chen, H.S., Wu, H.A., and Lin, S.S. (2017). Graphene-piezoelectric material heterostructure for harvesting energy from water flow. Adv. Func. Mater. *27*, 1604226.

Zhu, G., Lin, Z.H., Jing, Q.S., Bai, P., Pan, C.F., Yang, Y., Zhou, Y.S., and Wang, Z.L. (2013). Toward large-scale energy harvesting by a nanoparticle-enhanced triboelectric nanogenerator. Nano Lett. *13*, 847–853.

ISCI, Volume *22*

Supplemental Information

Direct-Current Generator Based on Dynamic PN Junctions with the Designed Voltage Output

Yanghua Lu, Zhenzhen Hao, Sirui Feng, Runjiang Shen, Yanfei Yan, and Shisheng Lin

SUPPLEMENTAL FIGURES AND LEGENDS

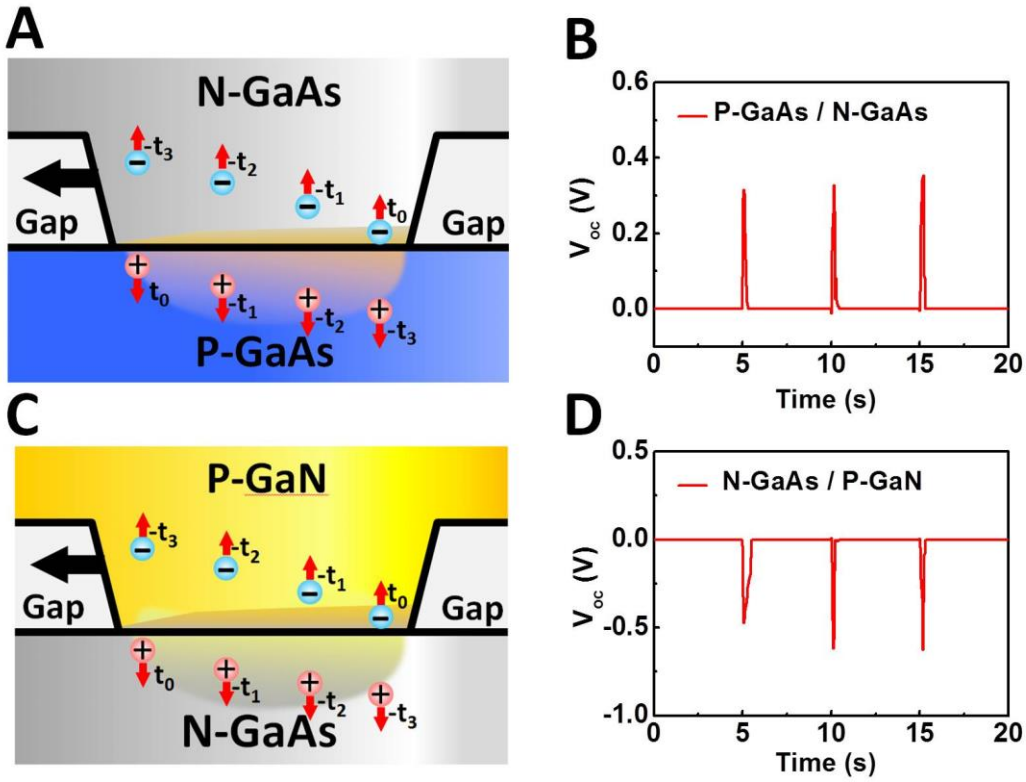

Figure S1. P-type GaAs and GaN used to reveal the distinctive current generation mechanism, related to Figure 1.

(A) Schematic diagram of dynamic P-GaAs/N-GaAs generator.

(B) V_{oc} of the dynamic P-GaAs/N-GaAs generator.

(C) Schematic diagram of the dynamic N-GaAs/P-GaN generator.

(D) V_{oc} of the dynamic N-GaAs/P-GaN generator.

The force is 6.0 N and the speed is 5.0 cm/s.

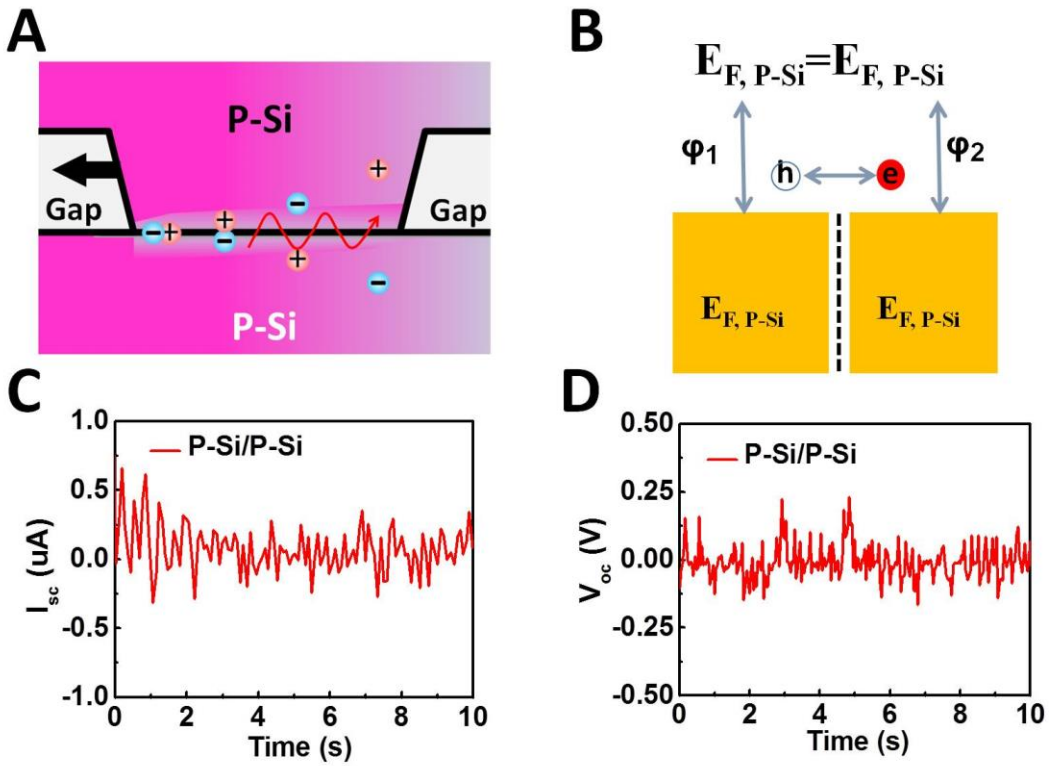

Figure 2. Dynamic P-Si/P-Si junction with same Fermi level, related to Figure 1.

(A) The schematic diagram of the dynamic P-Si/P-Si junction.

(B) One-dimensional band diagram of the P-Si/P-Si junction.

(C) The I_{sc} of the dynamic P-Si/P-Si generator with a 6.0 N force, a speed of 5.0 cm/s.

(D) The V_{oc} of the dynamic P-Si/P-Si generator with a 6.0 N force, a speed of 5.0 cm/s.

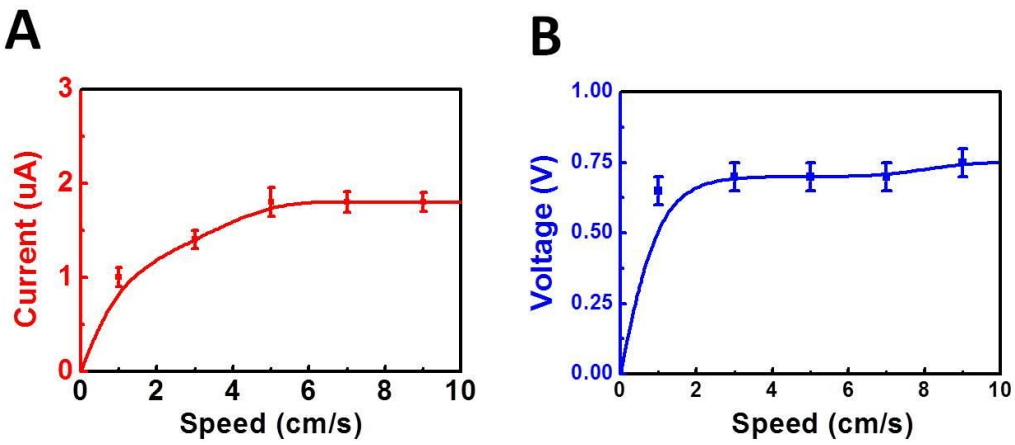

Figure 3. The role of speed on the output of dynamic PN generator, related to Figure 1.

(A) The V_{oc} of dynamic P-Si/N-GaAs generator in different speed with a 6.0 N force. The work area is 1.0 mm^2

(B) The I_{sc} of dynamic P-Si/N-GaAs generator in different speed with a 6.0 N force. The work area is 1.0 mm^2

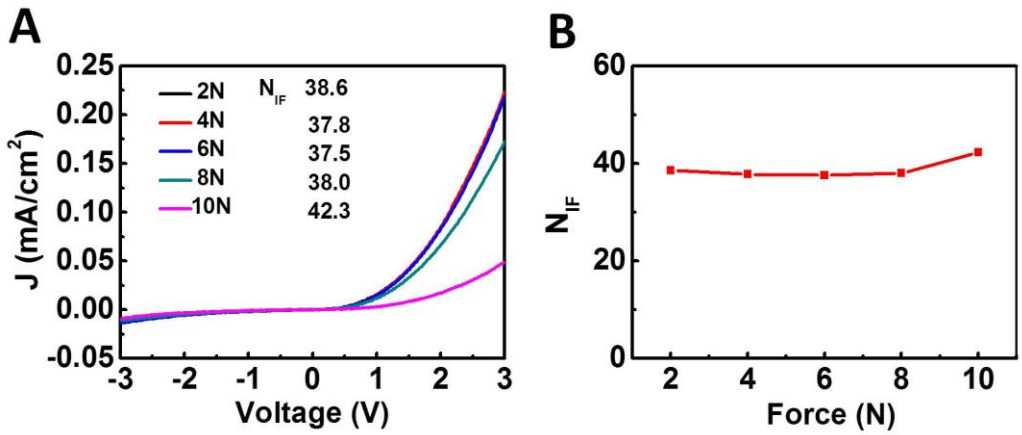

Figure 4. The role of force on the electrical properties of junction, related to Figure 1.

(A) Current-voltage curves of P-Si/N-GaAs junction under different forces. The N_{IF} is simulated from the I-V curve from 0 to 3V.

(B) N_{IF} of P-Si/N-GaAs junction under different forces. The N_{IF} is simulated from the I-V curve from 0 to 3V.

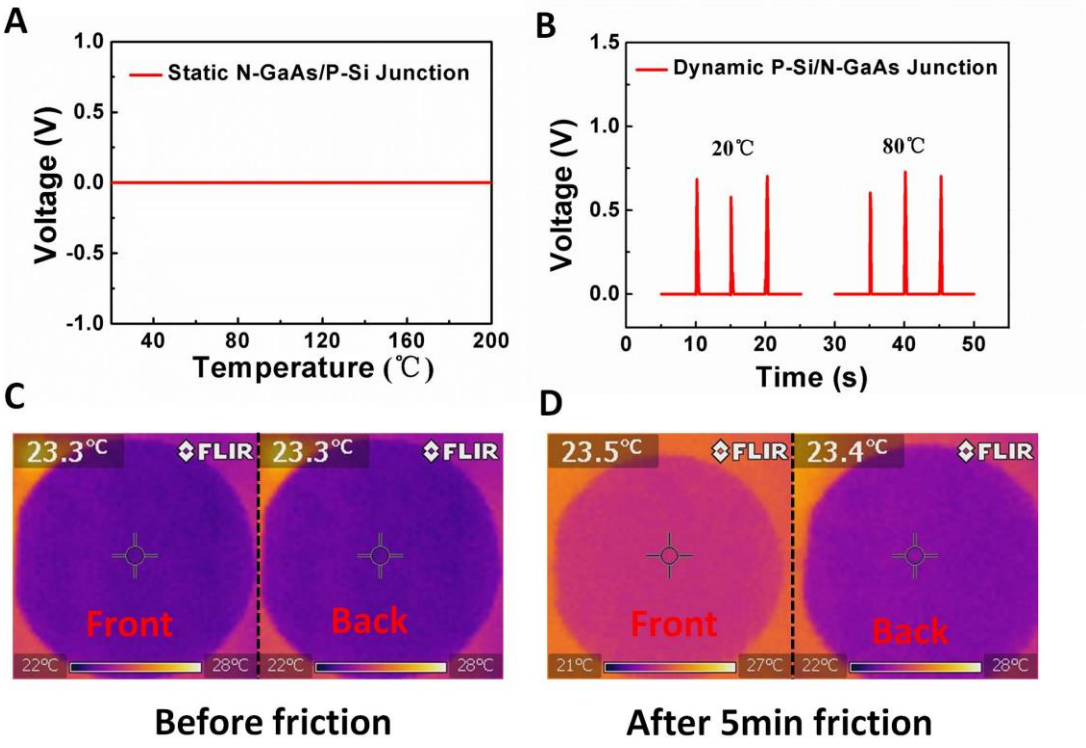

Figure 5. The role of heat generated by the friction between two semiconductors, related to Figure 2.

(A) The voltage output of static N-GaAs/P-Si junction with the temperature increased from 20 to 200 ℃.

(B) The voltage output of dynamic N-GaAs/P-Si junction with the temperature of 20 ℃ and 80 ℃.

(C) The temperatures of 4-inch P-Si wafer both the front and back side before friction.

(D) The temperatures of 4-inch P-Si wafer both the front and back side after 5 minutes friction.

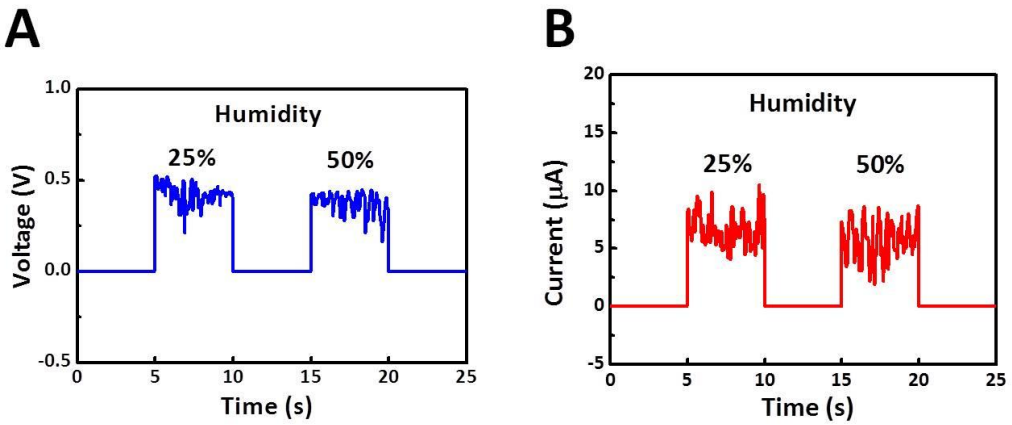

Figure 6. The role of humidity environment in the output of dynamic PN generator, related to Figure 2.

(A) The voltage output of the dynamic P-Si/ MoS_2 generator in different humidity environment of 25% and 50%.

(B) The current output of the dynamic P-Si/ MoS_2 generator in different humidity environment of 25% and 50%.

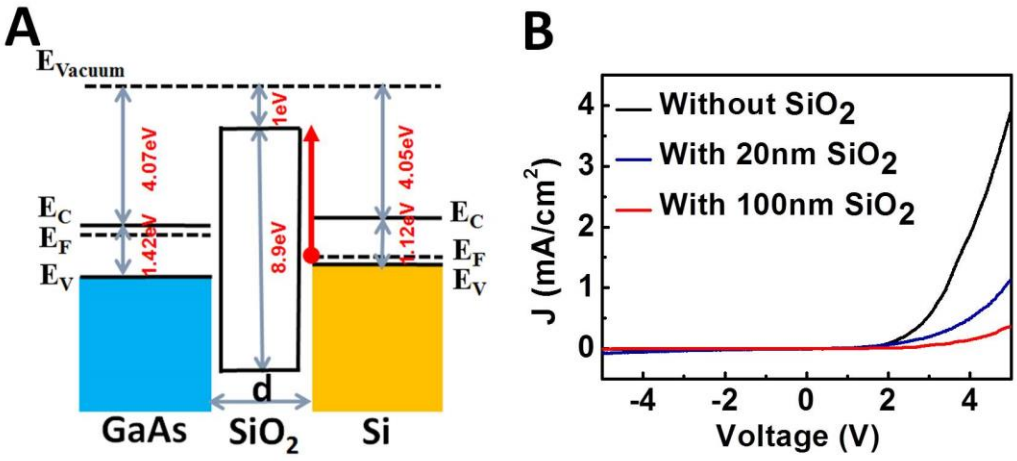

Figure 7. The detailed analyses of the P-Si/SiO_2/N-GaAs junction, related to Figure 2.

(A) One-dimensional band diagram of the P-Si/SiO_2/N-GaAs junction.

(B) J-V curves of the dynamic P-Si/N-GaAs generator without SiO_2 and with 20/100 nm SiO_2.

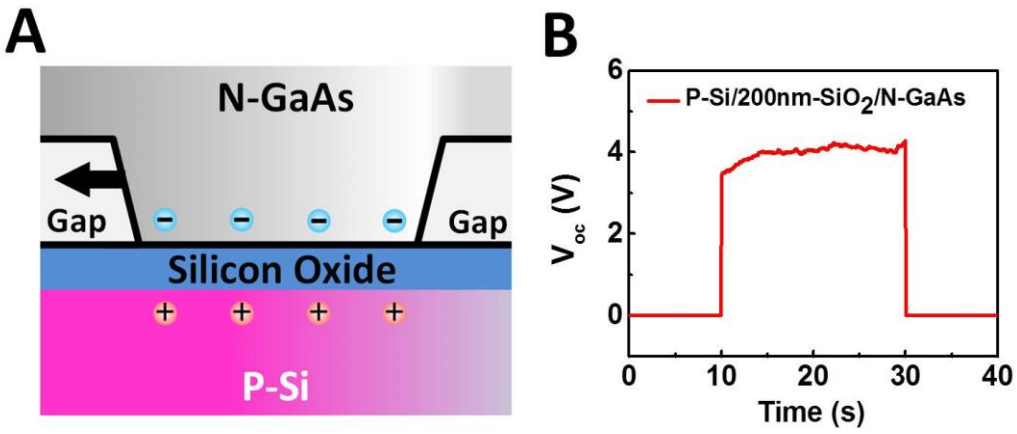

Figure 8. The voltage output of the P-Si/SiO_2/N-GaAs generator, related to Figure 2.

(A) The schematic diagram of P-Si/200nm-SiO_2/N-GaAs generator. The force is 6.0 N and the speed is 5.0 cm/s.

(B) The V_{oc} of P-Si/200nm-SiO_2/N-GaAs generator. The force is 6.0 N and the speed is 5.0 cm/s.

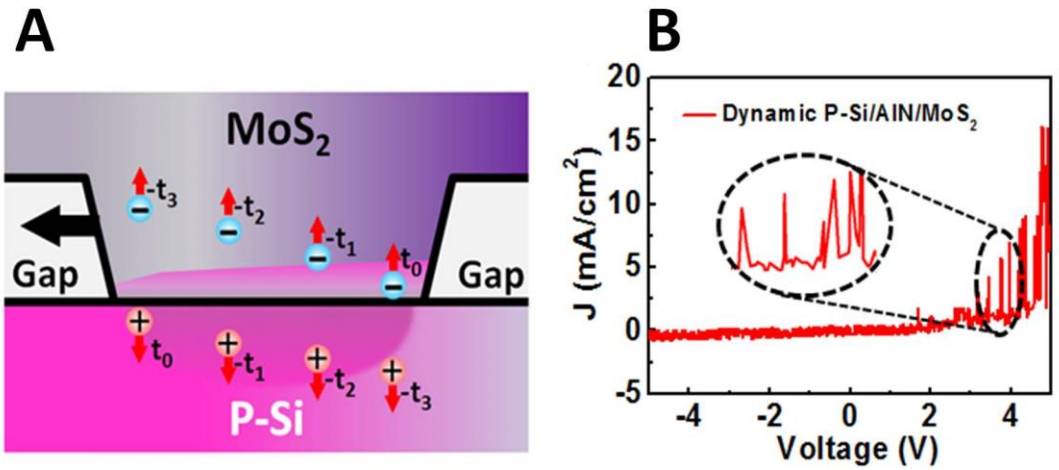

Figure 9. The interfacial carrier dynamic process of the P-Si/AlN/MoS_2 generator, related to Figure 3.

(A) The schematic diagram of the dynamic P-Si/AlN/MoS_2 generator.

(B) The J-V curve of the dynamic P-Si/AlN/MoS_2 junction with a 6.0 N force. The contact area is 0.05 mm^2.

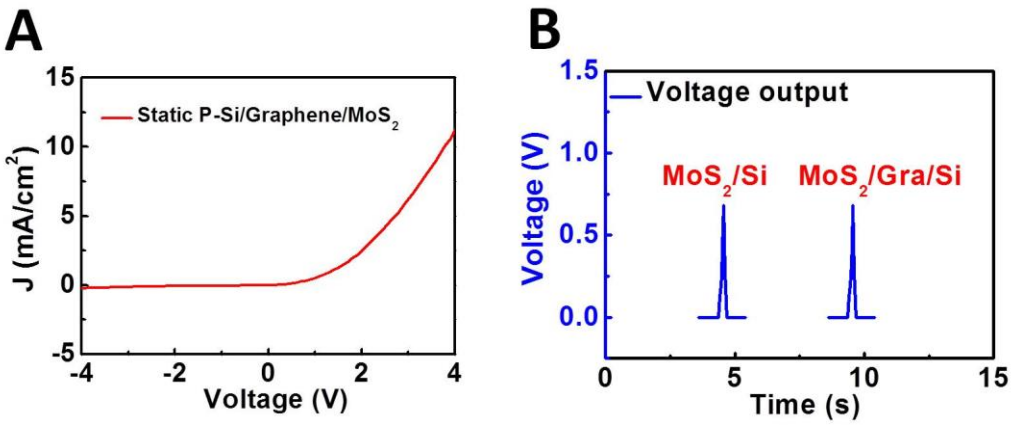

Figure 10. The electrical properties of dynamic P-Si/Graphene/MoS_2 junction, related to Figure 3.

(A) The J-V curve of the dynamic P-Si/Graphene/MoS_2 junction with a 6.0 N force.

(B) The voltage output of dynamic MoS_2/Si and MoS_2/Graphene/Si generator.

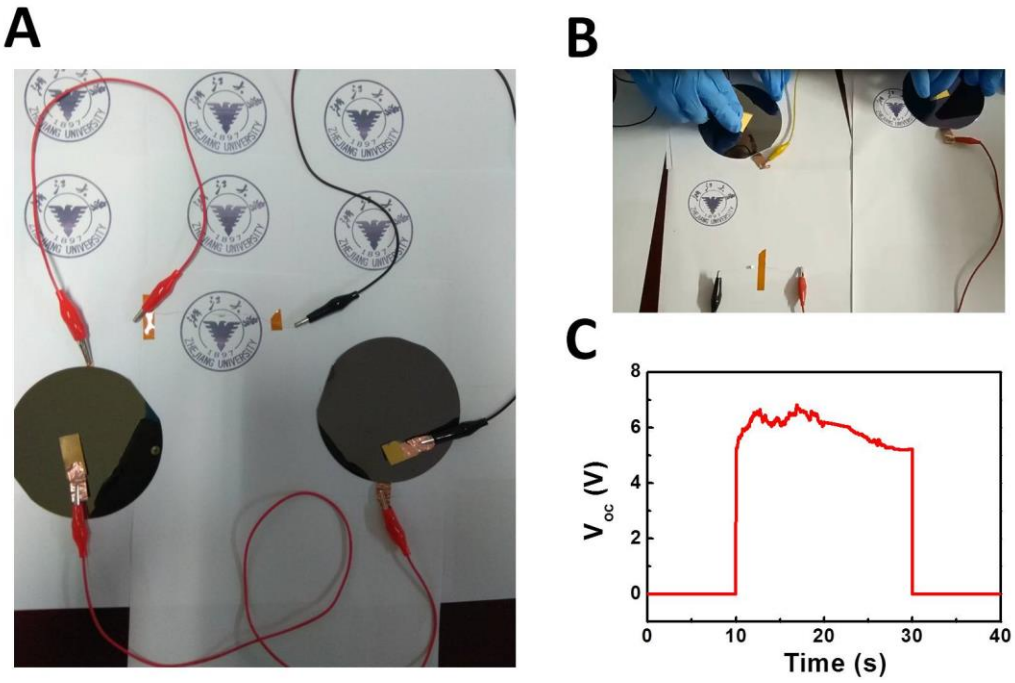

Figure 11. Experiment to light up a blue LED without any external rectifying circuits and energy storage units directly, related to Figure 4.

(A) The captured optical picture of the LED lighting experiment.

(B) The working dynamic PN generator.

(C) The V_{oc} output achieved under work of two generators with a 6.0 N force, a speed of 5.0 cm/s.

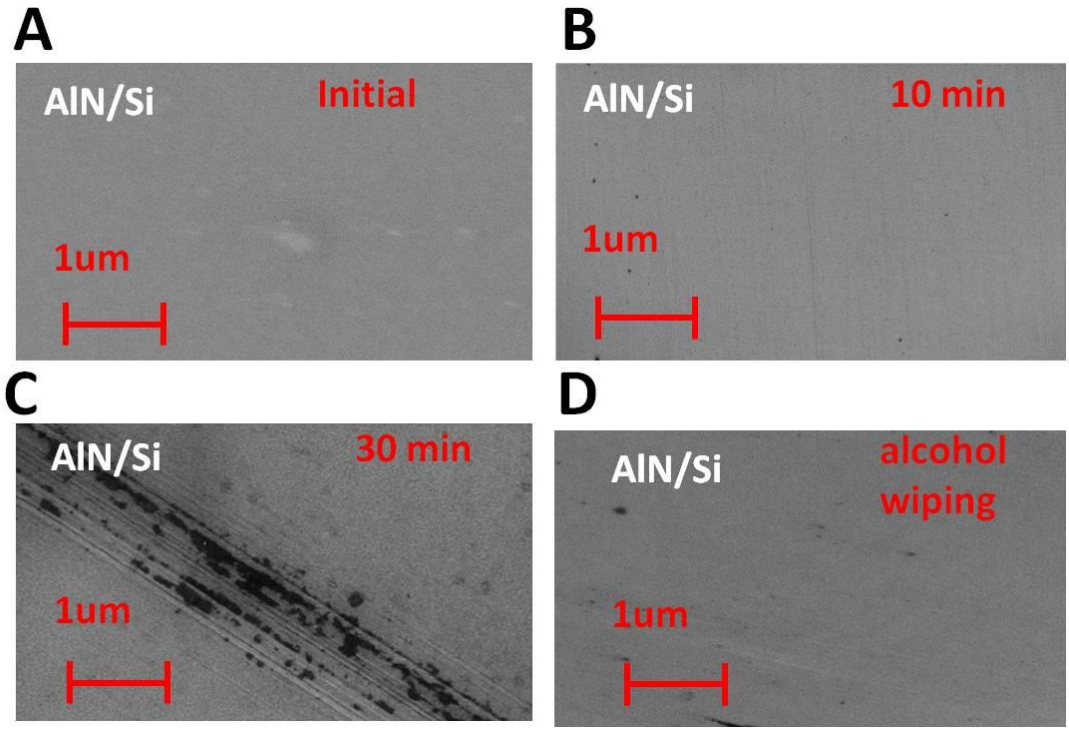

Figure 12. SEM images of the P-Si/AlN surface at different time points, on the scale of 1μm. The irregularly black object is the residual lamellar MoS_2 in the surface of AlN/P-Si surface, related to Figure 4.

(A) SEM images of the AlN/P-Si surface at initial state.

(B) SEM images of the AlN/P-Si surface after sliding for 10min.

(C) SEM images of the AlN/P-Si surface after sliding for 30min.

(D) SEM images of the AlN/P-Si surface after alcohol wiping.

TRANSPARENT METHODS

Devices fabrication

Firstly, the double side polished N-type GaAs wafer was dipping into 10 wt% HCl for 10 minutes to remove the native oxide layer in the surface and washed by deionized water. Then Ti/Au (20 nm/100 nm) electrode was fabricated with magnetron sputtering on one side of GaAs wafer. Similarly, the single side polished P-type and N-type Si substrate were dipping into 10 wt% HF for 10 minutes to remove the native oxide layer in the interface and then washed by deionized water. The MoS_2 flake was stripped by micromechanical force. Ti/Au (20 nm/50 nm) electrode was fabricated with magnetron sputtering on the unpolished side of Si substrate and MoS_2 flake. The thickness of the MoS_2 flake was measured as 0.3 mm. The N-type GaAs or MoS_2 was pressed closely on the P-type Si substrate by the hand, making sure a solid electrical contact between N-type GaAs/MoS_2 and P-type Si substrate can be achieved. The SiO_2 layer on P-type Si is fabricated with thermal oxidation method in 1100℃. The AlN layer on P-type Si is fabricated with physical vapor deposition method. The HfO_2, Al_2O_3 and ZnO layer on P-type Si is fabricated with atomic layer deposition method. The graphene layer is grown on copper foil by chemical vapor deposition technique, which can be transferred to Si substrate with wet transfer method.

Physical characterization methods

The microscopic image of the generator was characterized with ZEISS optical microscopy. The current-voltage (I-V) curve of the PN junction was measured with Keithley 2400 system. The real-time voltage and current output were recorded in real

time by a Keithley 2010 system, which was controlled by a LabView-based data acquisition system with a sampling rate of 25 s^{-1}. The Keithley 6485 picoammeter was also used to verify accuracy of current output, which was controlled by a LabView-based data acquisition system with a sampling rate of 100 s^{-1}. We have designed a customized system to control the force and speed. For the linear mode, two different types of semiconductors are fixed on the desktop and pressure meter respectively. The pressure meter is fixed in a sliding rail and can move horizontally under the control of a microcontroller unit (MCU). There is a driving motor in the sliding rail, which is used to drive the pressure meter. So the semiconductor in the pressure meter can move horizontally and keep the same moving speed under the control of MCU. As for the circularly rotating work mode, we fix the driving motor in the edge of pressure meter and a mechanical arm is added. For the linear mode, the pressure and speed can be accurately controlled with a fluctuation of 5%. For the circularly rotating mode, the pressure and speed varies in a wider range as the inherent mechanical error such as the flatness of the mechanical arm and frame.

The Fermi level of GaAs and Si substrate

The Fermi level of the semiconductor can be calculated by the formula below as below:

$$E_{F-N} \approx E_i + k_B T \ln \frac{N_D - N_A}{n_i} \quad (1)$$

$$E_{F-P} \approx E_i - k_B T \ln \frac{N_A - N_D}{n_i} \quad (2)$$

where E_i is the middle value of the band gap, k_B is the Boltzmann constant, T is the temperature, n is the electron concentration and p is the hole concentration. The n_i is

the intrinsic carrier concentration of the semiconductor. $E_{F\text{-}N}$ and $E_{F\text{-}P}$ are the Fermi level of the N-type and P-type semiconductors we used. The electron concentration and intrinsic carrier concentration of the N-type GaAs substrate used here is 5×10^{17} cm^{-3} and 1.8×10^{6} cm^{-3}, respectively. The conduction and valence band of N-type GaAs locate 4.07 eV and 5.49 eV below the vacuum energy level, respectively (Vurgaftman et al., 2001). Therefore, the Fermi level of the N-type GaAs is calculated as 4.10 eV based on equation (1). The electron concentration and intrinsic carrier concentration of the N-type GaN substrate used here is 1×10^{18} cm^{-3} and 3.26×10^{10} cm^{-3}, respectively. The conduction and valence band of N-type GaN locate 3.1 eV and 6.49 eV below the vacuum energy level, respectively (Vurgaftman et al., 2001). Therefore, the Fermi level of the N-type GaN is calculated as 4.35 eV based on equation (1).

Similarly, the hole concentration and intrinsic carrier concentration of the P-type Si substrate used here is 4.34×10^{18} cm^{-3} and 1.5×10^{10} cm^{-3}, respectively. The conduction and valence band of P-type Si locate 4.05 eV and 5.17eV below the vacuum energy level, respectively (Sze, 1981). Therefore, the Fermi level of the P-type Si is calculated as 5.12 eV based on equation (2). On the other hand, The electron concentration and intrinsic carrier concentration of the N-type Si substrate used here is 4.63×10^{15} cm^{-3} and 1.5×10^{10} cm^{-3}, respectively. Therefore, the Fermi level of the N-type Si is calculated as 4.28 eV based on equation (1).

The N_{IF} of the GaAs/Si junction

The work function of N-type GaAs and P-type Si is approximate to its conduction band or valence band, i.e. 4.28 eV and 5.12 eV, respectively. Thus a built-in electric field will form between the N-GaAs and P-Si substrate normally. When N-type GaAs touches P-type Si substrate by a constant force, electrons of the N-type GaAs will inject into P-type Si and a depletion region will form in the interface. The N_{IF} of GaAs/Si junction can be extracted by fitting dark J-V curves, which can be written as follows:

$$J = J_0(exp\frac{qV}{N_{IF}KT} - 1) \quad (3)$$

where K is the Boltzmann constant, T is the temperature and N_{IF} is the ideality factor. According to the thermionic-emission theory, J_0 is the reverse saturation current density.

The simulation of the experimental current density as a function of electric field

It is noteworthy that the generation of the current and voltage is caused by the rebounding carriers in the interface of PN junction. The effect of bounding back is influenced by the barrier height of the interface barrier. With a large bandgap, SiO_2 thin layer could act as a tunneling barrier between GaAs and Si. The valence and conduction band of SiO_2 has been tilted to form a triangle barrier. And the bounding back hot carriers on the surface lead to favorable conditions for FN tunneling where the electric field is huge. At room temperature, the hole current as a function of the electric field can be described by the tunnelling Fowler–Nordheim mechanism:

$$J = BE^2 exp\left(\frac{-D(m^*\phi^3)^{1/2}}{E}\right)$$

$$\mathrm{B} = \frac{q^3}{(8\pi h\phi)}, D = \frac{8\pi\sqrt{2}}{(3hq)}, E = V/d$$

where q is the electron charge, h is Planck's constant, m^* is the hole effective mass, ϕ is the barrier height at the P-i-N junction interface, E is the electric field across the junction, V is the voltage of the device and d is the thickness of the insulating layer. In the effect of the tunneling, the voltage output is less than the semiconductor-insulating layer barrier height when the insulating layer is thin. However, with the increase of dielectric layer thickness, the hopping or defect assisted tunneling become the leading factor of current generating. Hot and high energy electrons will still transfer across the interface through hopping effect while electrons with lower energy will be hindered for passing the thick layer, thus a much lower current density was observed for the case of thick SiO_2 existed at the interface between P and N semiconductor. The high energy hot electrons are caused by the severely bounding back effect by the large internal field at the interface, leading to the current response even when the SiO_2 layer as high as 200nm. Both the tunneling and hopping effects are positive correlated with the electric field E. With the decrease of electric field E, the possibility of hot electrons tunneling or hopping across the interface is exponentially decaying, leading the decrease of the current output. A simulation of the experimental current density as a function of electric field is achieved: $J = 1.73 - 1.79 \times e^{-\frac{E}{393000}}$. It well supports the exponential decay rule of the output current while the thickness of insulating layer increases, which demonstrates that hopping related transport or other tunneling process are the main factors in our dynamic P-i-N junction system.

The energy-conversion efficiency of the moving Si/AlN/MoS_2 junction generator

The working circuit is consisted of a series resistance (R_s), a recombination generated parallel resistance (R_p) and a load resistance (R_L). An increasing voltage and decreasing current density can be measured with the increase of load resistance. The power conversion efficiency of the dynamic PN junction generator can be expressed as below:

$$\mathrm{PCE} = \frac{P_{max}}{P_{in}} = \frac{V_{oc} \times J_{sc} \times FF}{P_{in}} = \frac{V_{max} \times J_{max}}{P_{in}} = \frac{V_{max} \times J_{max}}{F \times v}$$

$$\mathrm{FF} = \frac{V_{max} \times J_{max}}{V_{oc} \times J_{sc}}$$

where V_{oc} is the open-circuit voltage of the generator, J_{sc} is the short-circuit current density of the generator. FF is the fill factor of the generator. And V_{max} is the working voltage of the generator under the maximum power output, J_{max} is the working current density of the generator under the maximum power output. F is the force of friction between two semiconductors, v is the moving speed of the semiconductor wafer. We should emphasize that our output power is calculated with the average working voltage and current density of the direct-current generator in 8.0s and 200 points. For the dynamic Si/AlN/MoS_2 junction generator in the manuscript, V_{oc} and J_{sc} are as high as 5.1V and 112A/m^2, as shown in Figure R17d. However, the work voltage, current and power density are changed with the electrical load R. Specifically, the peak power output (P_{max}) of 130W/m^2 can be found around R≈360kΩ, of which the R value is close to the internal resistance r of the power generation unit. And the energy-conversion efficiency of the moving Si/AlN/MoS_2 junction generator can be calculated to be about 32.5%.

Moreover, for this dynamic Si/AlN/MoS_2 junction generator, the current density of 112.0 A/m^2 is orders of magnitude higher than triboelectric nanogenerators (~10^2 times) and piezoelectric nanogenerators (~10^3 times), which can be further enhanced through optimizing the PN junction interface and structure. For the dynamic Si/AlN/MoS_2 junction generator, the work mechanism is based on the built-in electric field bounding back diffusing carriers in dynamic PN junctions, breaking up the equilibrium between drift and diffusion current in the PN junction. So this generator has the advantage of converting mechanical energy into direct current electricity continuously in ultrahigh current density without rectifying circuit, which breaks through the limitation of discharging process in short-circuiting condition.

REFERNCES

Vurgaftman, I., Meyer, J.R. & Ram-Mohan, L.R. (2001). Band parameters for III–V compound semiconductors and their alloys. J. Appl. Phys. **89**, 5815-5875.

Sze, M.S. (1981). Physics of Semiconductor Devices 2nd Ed. Wiley, New York.